Rare Metal Materials and Engineering
Volume.50, Issue.4, April 2021
Available online at **www.rmme.ac.cn**

Science Press

Cite this article as: Xu Tongzhou, Pan Xiuhong, Zhang Minghui, et al. In-situ Observation of Shrinkage Formation and Its Mechanism During Ni-based CMSX-4 Superalloy Solidification[J]. Rare Metal Materials and Engineering, 2021, 50(04): 1113-1117.

In-situ Observation of Shrinkage Formation and Its Mechanism During Ni-based CMSX-4 Superalloy Solidification

Xu Tongzhou[1,2], Pan Xiuhong[1], Zhang Minghui[1], Tang Meibo[1], Li Huidong[1], Liu Xuechao[1]

[1] Shanghai Institute of Ceramics, Chinese Academy of Sciences, Shanghai 200050, China; [2] China Innovation Academy of Intelligent Equipment Co., Ltd, Ningbo 315700, China

Abstract: Confocal laser scanning microscope (CLSM) was used to study the solidification behavior of a nickel-based single crystal superalloy CMSX-4 in real time. SEM and EDS were used to investigate the micromorphology and element segregation characteristics of the solidified samples. Shrinkage and carbide formation were observed during alloy solidification. Results show that three types of shrinkage are found, including square, pentagonal star and angular shrinkages. The formation mechanism of the three types of shrinkage is discussed, which is related to the shape of the enclosed area surrounded by secondary dendrite arms growing in different directions. In addition, carbides are comprised of two forms, namely, flocculent and lath carbide. Hf elements are enriched in flocculent carbides, while Cr elements are enriched in lath carbides.

Key words: in-situ observation; CMSX-4; shrinkage; carbide; solidification mechanism

Shrinkage is a common defect found in metal alloy castings. It can be caused through separation of molten metal into discrete pools during the casting process after the metal alloy solidifies. As the molten pool cannot be compensated by feed metal, it will cause defects[1-4]. During the process of directional solidification of Ni-based superalloys, impurities will enter the alloy, changing the mode of solidification and producing shrinkage[5-7]. At the inner surface of the mold shell, shrinkage can also occur due to interactions between the liquid alloy and the shell. The occurrence of shrinkage will reduce the fatigue strength, yield strength and high temperature creep properties of single crystal nickel-based superalloys[8-12].

CMSX-4 is a second generation nickel-based single crystal superalloy and is widely used during manufacture of heavy-duty gas turbine blades[13-15]. Due to increasing requirements for the use of gas turbine blades, improving the mechanical properties of this superalloy has becoming increasingly important. Reducing the occurrence of holes and defects caused by shrinkage is one of the most effective ways to improve the mechanical properties of alloys[16]. Many studies have demonstrated reduced number and volume of shrinkage in CMSX-4 superalloy through introducing a magnetic field[17], using hot isostatic pressing technology[18], thermal regeneration treatment[19,20] and other processing methods. Nevertheless, defects caused by shrinkage (or voids) are still inevitable during the preparation of nickel-based superalloy. Generally, research on the mechanism of shrinkage porosity is performed through undertaking structural analysis after solidification[21-23]. However, there are several studies that investigate shrinkage in-situ with mechanisms proposed after analyzing the solidification process[24-26].

In the present study, the solidification of CMSX-4 nickel-based superalloy was studied in-situ by CLSM observation. In contrast to previous studies where only the available surface solidification of the alloy melt can be observed, this investigation will cover the surface of the alloy with a transparent sapphire, so that the sapphire acts as a mold and induces the sapphire during the alloy solidification process. During solidification, shrinkage will occur and this will also be studied to determine the shrinkage porosity and formation mechanism.

Received date: April 13, 2020
Foundation item: Ministry of Major Science & Technology of Shanghai (19DZ1100703); National Natural Science Foundation of China (51472263); Shanghai Institute of Ceramics, Chinese Academy of Sciences Launched the Fund in Advance (Y82ZC8180G); Key Laboratory of Space Manufacturing, Chinese Academy of Sciences (SMT-2019-004)
Corresponding author: Pan Xiuhong, Ph. D., Associate Professor, Shanghai Institute of Ceramics, Chinese Academy of Sciences, Shanghai 200050, P. R. China, E-mail: xhPan@mail.sic.ac.cn

1 Experiment

CMSX-4 nickel-based single crystal superalloy was selected as the alloy to be investigated. The chemical composition of the alloy is presented in Table 1. The size of the experimental sample examined was 5 mm×5 mm×0.5 mm. Alloy samples were prepared by polishing the surface with sandpaper until no scratches could be observed. Thereafter, the sample was cleaned in alcohol solution using an ultrasonic bath. Before melting and solidification experiments were conducted, the solidification point was measured by differential scanning calorimeter (DSC), operated at a cooling rate of 30 °C/min.

A polished alloy sample was heated in an Al_2O_3 crucible by halogen lamp and the morphology of the upper surface was observed by CLSM. A transparent sapphire sheet of Φ6 mm× 0.3 mm was placed on the surface of the sample to act as a mold shell, whilst also allowing observation during the heating process. The sample temperature was raised to 1450 °C and maintained for 5 min to ensure that the sample was completely melted. Following this the temperature was dropped to 1000 °C at a rate of 30 °C/min, as seen in Fig.1. Throughout the duration of the experiment, high-purity argon gas was introduced to protect the sample.

Ultrasonic cleaning was performed on the sample after the in-situ observation. A Magellan 400 scanning electron microscope (SEM) was operated at 20 keV in high current mode with a 120 um aperture used in back-scatter mode to verify the composition and phase relationships. An Oxford energy dispersive spectroscopy (EDS) system attached to the microscope was used for elemental analysis. A Cu standard was used to calibrate the EDS system for quantitative analysis.

2 Results and Discussion

2.1 Mechanism of shrinkage formation

Fig.2 presents the DSC curve obtained when heating the

Table 1 Chemical composition of CMSX-4 superalloy（wt%）

Cr	Co	Mo	W	Ta	Re	Al	Ti	Hf	Ni
6.5	9.0	0.6	6.0	6.5	3.0	5.6	1.0	0.1	Bal.

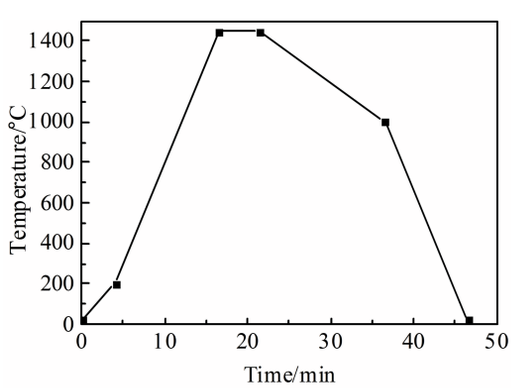

Fig.1 Temperature-time curve of CMSX-4 superalloy during observation

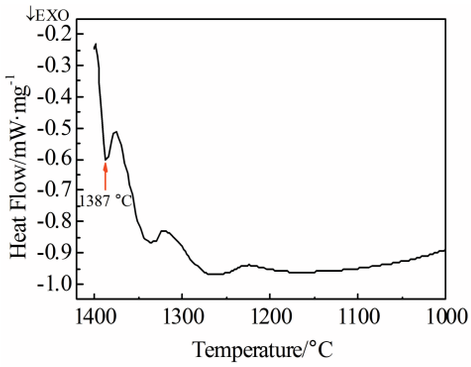

Fig.2 DSC curve of the CMSX-4 superalloy with decreasing the temperature

CMSX-4 superalloy. As the temperature gradually increases, the entropy value of the sample gradually concurrently increases, and the sample begins to melt at 1376.9 ℃. After reaching 1400 ℃, the temperature was decreased. When the temperature reaches 1387 ℃, a peak was measured, as a indicative of the freezing point of CMSX-4.

During in-situ observation of the alloy, the sample was heated to 1450 °C and kept for 5 min, followed by cooling at a rate of 30 °C/min. During this process, the central area of the sample surface was directly observed by confocal laser scanning microscope. Fig. 3 presents the results of observation. When the sample reaches 1450 °C, it is in a molten state (Fig.3a). In addition, it is observed that a small amount of bubbles are mixed between the sapphire and the melt. As the melt temperature decreases to 1352.3 °C, a square bubble is generated, as indicated by the arrow in the lower right corner of Fig.3b, and it is observed to extend outward from the corners (Fig.3c). Extension of the corners may be a channel to connect adjacent bubbles. As the temperature continues to decrease, the left end of the square bubble extends out of the channel, and a five-pointed star bubble forms. This bubble also continues to grow and extends outward (Fig.3d). When the temperature is lower than 1337.6 ℃, shrinkage forms (Fig.3f).

In Fig.3f, it can be observed that square bubbles are generated due to two pairs of dendrite arms growing in opposite directions, forming a square shaped molten pool. As the dendrite arm shrinks during the solidification process, the molten metal in the pool will shrink into the dendrite arm and eventually form bubbles. The formation of five-pointed star-shaped bubbles is attributed to molten pool surrounded by five dendritic arms in three directions. When the molten metal in the pool is completely filled into the dendrite arms, five-point star-shaped bubbles are formed.

During observation via CLSM, evidence for angular shrinkage is found, as demonstrated in Fig.3g. This is potentially due to several secondary arms growing to one point from three different directions. However, these secondary arms will inhibit each other's growth processes, so they are unlikely to connect to each other. Due to this scenario, an angular molten pool is generated. After the growth of dendrite

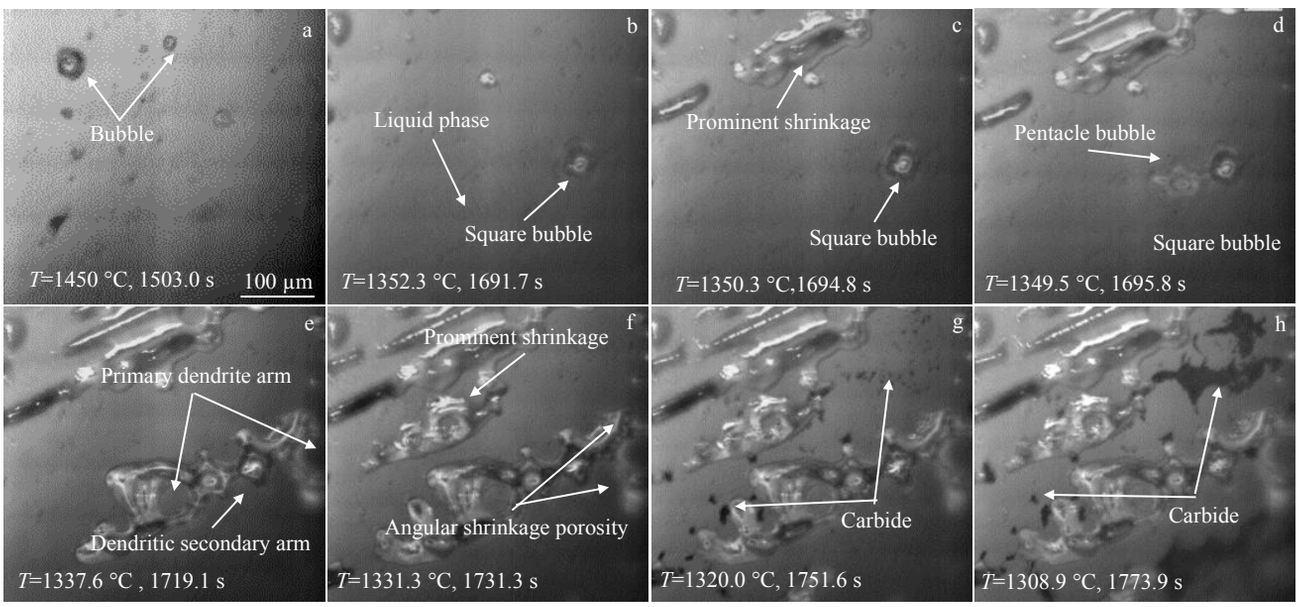

Fig.3 CMSX-4 superalloy solidification process in-situ observed by CLSM at different temperatures and time: (a) 1450 °C, 1503 s; (b) 1352.3 °C, 1691.7 s; (c) 1350.3 °C, 1694.8 s; (d) 1349.5 °C, 1695.8 s; (e) 1337.6 °C, 1719.1 s; (f) 1331.3 °C, 1731.3 s; (g) 1320.0 °C, 1751.6 s; (h) 1308.9 °C, 1773.9 s

arms is completed, an angular shrinkage forms [27].

When the temperature reaches 1320 °C, shrinkage growth is retarded as the dendrite arm is filled. Nevertheless, carbides begin to precipitate from the inside of the sample to the surface. Most of the carbides precipitate in proximity to the shrinkage, as shown in Fig.3h and 3i.

The area of shrinkage at different periods was measured by AUTOCAD software, and ORIGIN software was used to plot the relationship of shrinkage volume fraction versus time (Fig.4). The shrinkage score obtained can be divided into seven line segments and four stages. The red line indicates the slow growth stage, the green line is the mutation stage, the black line is the gentle stage, and the blue line is the end stage of solidification. The slope of the first and second mutation stages is 0.067 and 0.071, respectively.

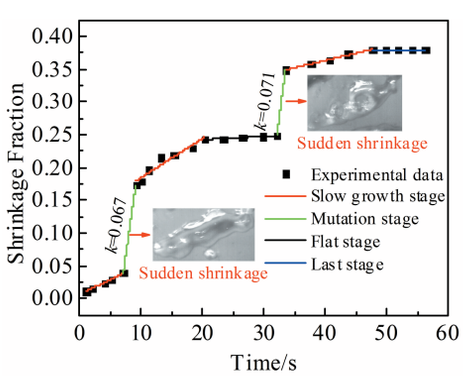

Fig.4 Curve of shrinkage volume fraction with time for CMSX-4 superalloy

During the initial stage of solidification (1~9.1 s), only a small amount of bubbles are generated in the melt and the rate of shrinkage fraction increase is comparatively small. This period corresponds to Fig.3b. During the period of 9.1~10.1 s, a large area of shrinkage is measured, resulting in an increase in the rate of shrinkage fraction generation (Fig.3c).

Over the time period of 10.1~20.3 s, the shrinkage and the five-pointed star bubble continues to grow (Fig.3d and 3e). Over the period of 20.3~32.1 s, the shrinkage area effectively maintains a similar shrinkage fraction, with almost no increase (Fig.3f). It is proposed that the shrinkage area stagnation during this period is primarily due to the slow absorption rate of the molten metal in the nearby small pool by the secondary arm inside the melt. The flow rate of the molten metal in the melt is greater than the speed, at which the metal is absorbed, thereby delaying the formation of shrinkage.

As growth of the secondary arm reaches the final stage, the small molten pool in proximity is completely divided. The molten metal in the pool continuously feeds into the secondary arm, but no flowing molten metal shrinks into the molten pool, as shown in Fig.3g. A large change in the slope of the shrinkage fraction occurs suddenly during the period of 32.1~33.5 s.

Over the interval of 33.5~44.7 s, the shrinkage volume in some areas increases slightly. When the duration of experimental observation reaches 44.7 s, the shrinkage volume no longer increases and carbides begin to precipitate, thus ending the solidification process.

2.2 Microstructure and morphology

During in-situ observation, CLSM's stereo imaging ability is superior to standard optical microscopes. However, the

instrument poorly images areas with large depth of field and obvious bumps. To analyze the process of shrinkage porosity and carbides, the as-generated alloy sample was ultrasonically cleaned, and the surface morphology was investigated by SEM. Segregation on the surface was studied through element content mapping via EDS.

The SEM secondary electron image is shown in Fig. 5, demonstrating various morphological features previously observed through studies with CLSM. It can be seen that the square bubble is surrounded by two pairs of secondary arms. A five-point star-shaped bubble surrounded by five dendrite arms, and an angular contraction formed by the three dendrite arms were observed. These phenomena are consistent with those found during field observation, confirming the mechanism of alloy shrinkage.

Higher magnification imaging of the bottom shrinkage structure was undertaken (Fig.5b). It can be seen from the image that the shrinking bottom is composed of fine crystal grains. In comparison, the slightly protruding section is composed of relatively sharp small crystal grains. These sharp crystal grains are tightly aggregated, showing different stages of growth. The direction of these growth stages is to the left of the image, indicating that the melt flow flows from the right to the left end.

Backscatter electron (BSE) imaging was used to observe carbides and evaluate their morphology, as shown in Fig.5c. In this image, bright white irregular carbides are also observed, and each individual aggregate is surrounded by a small volume of bubbles, inferring that the bubbles are related to formation of carbides. The SEM enlarged secondary electron image of the selected carbide area is shown in Fig.6a, with elemental mapping by EDS shown in Fig.6b. The bright white section in the picture is primarily composed of two structures, especially the flocculent structure at region 1 and the radial structure at region 2. Based on the elemental mapping of this alloy surface, the flocculent structure is mainly enriched in Hf with relatively low Ni elemental content. The data indicate that this area is mainly composed of HfC carbide[28,29]. The inner walls of the pores are enriched in Ni, Al, Cr. During solidification, Al and Cr are gathered near the pores due to the large temperature difference between the inner and outer walls of the bubble. This forms an intermetallic compound, and then carbides with enriched Cr and C elements in the proximity of bubbles form. However, Cr and Hf elements are not found to aggregate in the plane of the radial structure. The gray-black area is mainly composed of Ni-Al intermetallic compounds. A point test analysis was performed on the strip located in the radial structure. Segregation of Cr element in this area is more evident,

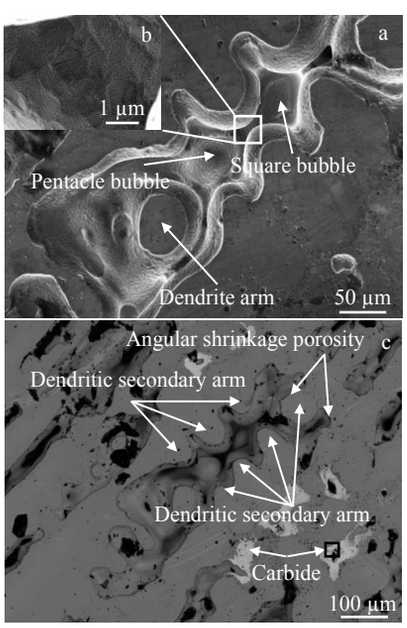

Fig.5 SEM-SE images of shrinkage (a) and grain (b) morphologies and BSE image (c) of shrinkage and carbide for CMSX-4 superalloy

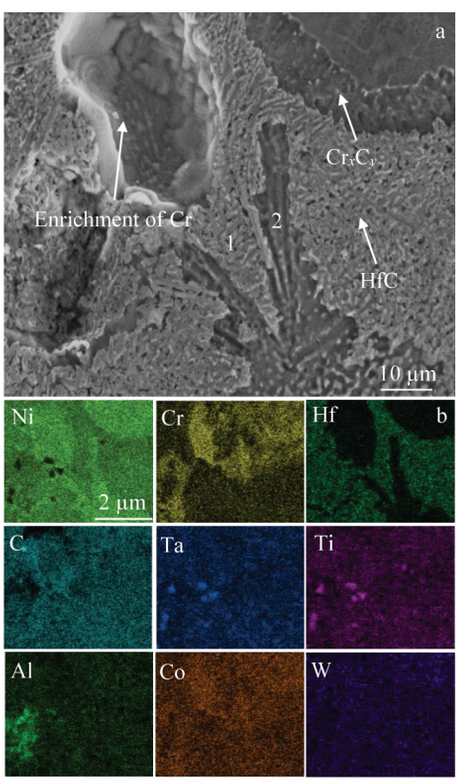

Fig.6 SEM morphology (a) and element mapping (b) of carbide for CMSX-4 superalloy

Table 2 EDS test results of carbide region marked in Fig.6a (wt%)

Location	Cr	Co	Mo	W	Ta	Re	Al	Ti	Hf	C
Region 1	3.47	5.82	0.27	0.60	6.98	-	5.04	1.41	22.58	11.26
Region 2	11.4	9.68	2.23	2.94	5.90	2.48	4.72	1.27	-	15.90

inferring that the strip structure is primarily Cr-rich carbide.

3 Conclusions

1) The solidification process of CMSX-4 can be studied by CLSM. Evidence for the mechanisms of shrinkage growth and carbide formation is found through observations and measurements during the solidification process.

2) Bubbles are generated after dendrite arms form a closed molten pool. The melt in the pool feeds these nearby dendrite arms, with bubbles generated.

3) Cracks and the formation of carbides are primarily at the inside of the sample toward the surface, and the location of the precipice is generally in the vicinity of shrinkage. The carbides are enriched in Hf and Cr. HfC carbide is mainly present as a flocculent structure and CrC carbide exists in a radial structure.

References

1 Srivastav A K, Murty B S. *Journal of Alloys and Compounds* [J], 2012, 536: 41

2 Wang J, Fu P, Liu H *et al*. *Materials & Design*[J], 2012, 35: 446

3 Ling Y, Zhou J, Nan H *et al*. *Journal of Manufacturing Processes*[J], 2017, 26: 433

4 Wu S P, Liu D R, Guo J J *et al*. *Journal of Alloys and Compounds*[J], 2007, 441: 267

5 Zheng L, Zhang G, Xiao C *et al*. S*cripta Materialia*[J], 2014, 74: 84

6 Eggeler Y M, Müller J, Titus M S *et al*. *Acta Materialia*[J], 2016, 113: 335

7 Liu K, Li Z, Wang J *et al*. *Materialia*[J], 2019, 8: 100 508

8 Li Q, Shen J, Qin L*et al*. *Journal of Materials Processing Technology*[J], 2019, 274: 116 308

9 Ruttert B, Meid C, Roncery L M *et al*. S*cripta Materialia*[J], 2018, 155: 139

10 Liu Y, Kang M, Wu Y *et al*. *Materials Characterization*[J], 2017, 132: 175

11 Prasad K, Sarkar R, Gopinath K *et al*. *Materials Science and Engineering A*[J], 2016, 654: 381

12 Graverend J B, Adrien J, Cormier J *et al*. *Materials Science and Engineering A*[J], 2017, 695: 367

13 Long H, Mao S, Liu Y *et al*. *Journal of Alloys and Compounds* [J], 2018, 743: 203

14 Huda Z, Edi P. *Materials & Design*[J], 2013, 46: 552

15 Xu W, Lu Z, Tian G *et al*. J*ournal of Materials Processing Technology*[J], *201*, 271: 615

16 Scholz A, Wang Y, Linn S *et al*. *Materials Science and Engineering A*[J], 2009, 510: 278

17 Li Q, Shen J, Qin L *et al*. *Journal of Alloys and Compounds*[J], 2017, 691: 997

18 Lan J, Xuan W, Han Y *et al*. *Journal of Alloys and Compounds* [J], 2019, 805: 78

19 Horst O M, Ruttert B, Bürger D *et al*. *Materials Science and Engineering A*[J], 2019, 758: 202

20 Wang H, Ning L Q, Tong J *et al*. *Rare Metal Materials and Engineering*[J], 2020, 49(1): 247

21 Yue Q, Liu L, Yang W *et al*. *Progress in Natural Science: Materials International*[J], 2017, 27: 236

22 Nawrocki J, Motyka M, Szeliga D *et al*. *Journal of Manufacturing Processes*[J], 2020, 49: 153

23 Jie Z, Zhang J, Huang T *et al*. *Journal of Alloys and Compounds*[J], 2017, 706: 76

24 Wang D, Lu X, Wan D *et al*. *Scripta Materialia*[J], 2019, 173: 56

25 Yan X, Xu Q, Liu B. *Journal of Crystal Growth*[J], 2017, 479: 22

26 Miao Z, Shan A, Wang W *et al*. *Transactions of Nonferrous Metals Society of China*[J], 2011, 21: 236

27 Plancher E, Gravier P, Chauvet E *et al*. *Acta Materialia*[J], 2019, 181: 1

28 Wang F, Xu W, Ma D *et al*. *Journal of Alloys and Compounds* [J], 2019, 792: 505

29 Han F, Wang X, Jia Y *et al*. *Materials Characterization*[J], 2020, 164: 110 329

原位观察镍基高温合金CMSX-4缩松形成过程及机理研究

许桐舟[1,2]，潘秀红[1]，张明辉[1]，汤美波[1]，李会东[1]，刘学超[1]

(1. 中国科学院上海硅酸盐研究所，上海 200050)

(2. 中机智能装备创新研究院(宁波)有限公司，浙江 宁波 315700)

摘　要：采用共聚焦激光扫描显微镜（CLSM）对镍基单晶高温合金CMSX-4的凝固行为进行实时观察。并利用扫描电镜（SEM）和能谱仪（EDS）对凝固样品的微观形貌和元素偏析特性进行研究。结果表明，在合金凝固过程中观察到缩松和碳化物的形成。缩松具有3种形态：方形缩松，五角星形缩松和角形缩松。并讨论了3种缩松的形成机理，缩松的形成机制主要与次级枝晶臂沿不同方向生长所包围的封闭区域的形状有关。另外，发现碳化物由2种形式组成，即絮状碳化物和板条状碳化物。絮状碳化物中富含Hf元素，而Cr元素被富集在板条状碳化物。

关键词：原位观察；CMSX-4；缩松；碳化物；凝固机理

作者简介：许桐舟，男，1995年生，硕士，中国科学院上海硅酸盐研究所晶体中心，上海　200050，E-mail：405186928@qq.com